The Mu2e Crystal and SiPM Calorimeter: Construction Status

Nikolay Atanov, Vladimir Baranov, Leo Borrel, Caterina Bloise, Julian Budagov, Sergio Ceravolo, Franco Cervelli, Francesco Colao, Marco Cordelli, Giovanni Corradi, Yuri Davydov, Stefano Di Falco, Eleonora Diociaiuti, Simone Donati, Bertrand Echenard, Carlo Ferrari, Ruben Gargiulo, Antonio Gioiosa, Simona Giovannella, Valerio Giusti, Vladimir Glagolev, Francesco Grancagnolo, Dariush Hampai, Fabio Happacher, David Hitlin, Matteo Martini, Sophie Middleton, Stefano Miscetti, Luca Morescalchi, Daniele Paesani, Daniele Pasciuto, Elena Pedreschi, Frank Porter, Fabrizio Raffaelli, Alessandro Saputi, Ivano Sarra, Franco Spinella, Alessandra Taffara, Anna Maria Zanetti, and Ren-Yuan Zhu, *Life Senior Member, IEEE*

***Abstract*— The Mu2e experiment at Fermilab searches for the neutrino-less conversion of a negative muon into an electron, with a distinctive signature of a mono-energetic electron with an energy of 104.967 MeV. The calorimeter is made of two disks of pure CsI crystals, each read out by two custom large-area UV-extended silicon photomultipliers (SiPMs). It plays a fundamental role in providing excellent particle identification capabilities and an online trigger filter while improving the track reconstruction, requiring better than 10% energy and 500 ps timing resolutions for 100 MeV electrons. In this article, we present the status of construction and the quality control (QC) performed on the produced crystals and photosensors, the development of the rad-hard electronics, and the most important results of the irradiation tests. Construction of the mechanics is also reported. Status and plans for the calorimeter assembly and its first commissioning are described.**

***Index Terms*— Calorimeter, charged lepton flavor violating (CLFV), crystal, CsI, SiPM.**

Manuscript received 14 November 2022; revised 7 March 2023 and 31 March 2023; accepted 31 March 2023. Date of publication 5 April 2023; date of current version 18 July 2023. This work was supported in part by the US Department of Energy; in part by the Istituto Nazionale di Fisica Nucleare, Italy; in part by the Science and Technology Facilities Council, U.K.; in part by the Ministry of Education and Science, Russian Federation; in part by the National Science Foundation, USA; in part by the National Science Foundation, China; in part by the Helmholtz Association, Germany; and in part by the EU Horizon 2020 Research and Innovation Program under the Marie Sklodowska-Curie Grant through Agreement 734303, Agreement 822185, Agreement 858199, Agreement 101003460, and Agreement 101006726. Fermilab is managed by Fermi Research Alliance, LLC (FRA), acting under Contract DE-AC02-07CH11359.

Nikolay Atanov, Vladimir Baranov, Julian Budagov, Yuri Davydov, and Vladimir Glagolev are with the Joint Institute for Nuclear Research, 141980 Dubna, Russia.

Leo Borrel, Bertrand Echenard, David Hitlin, Sophie Middleton, Frank Porter, and Ren-Yuan Zhu are with the California Institute of Technology, Pasadena, CA 91125 USA.

Caterina Bloise, Sergio Ceravolo, Marco Cordelli, Giovanni Corradi, Eleonora Diociaiuti, Ruben Gargiulo, Simona Giovannella, Dariush Hampai, Fabio Happacher, Stefano Miscetti, Daniele Paesani, and Ivano Sarra are with the Laboratori Nazionali di Frascati, INFN, 00044 Frascati, Italy (e-mail: eleonora.diociaiuti@lnf.infn.it).

Franco Cervelli, Stefano Di Falco, Carlo Ferrari, Antonio Gioiosa, Luca Morescalchi, Elena Pedreschi, Fabrizio Raffaelli, Franco Spinella, and Alessandra Taffara are with the INFN—Sezione di Pisa, 56127 Pisa, Italy.

Francesco Colao is with the Laboratori Nazionali di Frascati, INFN, 00044 Frascati, Italy, and also with the ENEA—Frascati, 00044 Frascati, Italy.

Simone Donati and Daniele Pasciuto are with the INFN—Sezione di Pisa, 56127 Pisa, Italy, and also with the Department of Physics, University of Pisa, Pisa, Italy.

Valerio Giusti is with the INFN—Sezione di Pisa, 56127 Pisa, Italy, and also with the Department of Civil and Industrial Engineering, University of Pisa, Pisa, Italy.

Francesco Grancagnolo is with the INFN—Sezione di Lecce, 73100 Lecce, Italy.

Matteo Martini is with the Laboratori Nazionali di Frascati, INFN, 00044 Frascati, Italy, and also with the Department of Engineering Sciences, Guglielmo Marconi University, 00193 Rome, Italy.

Alessandro Saputi is with the INFN—Sezione di Ferrara, 44122 Ferrara, Italy.

Anna Maria Zanetti is with the INFN—Sezione di Trieste, 34149 Trieste, Italy.

Color versions of one or more figures in this article are available at https://doi.org/10.1109/TNS.2023.3264757.

Digital Object Identifier 10.1109/TNS.2023.3264757

I. Mu2e Experiment and Charged Lepton Flavor Violation Processes

THE Mu2e experiment, under construction at Fermilab, will search for the charged lepton flavor violating (CLFV) process of a muon converting into an electron in the electric field of Al nuclei. The CLFV processes are forbidden in the Standard Model (SM) and even assuming its minimal extension, which allows neutrino oscillations, their branching ratio is completely negligible: BR $< 10^{-50}$ [2].

Any observation of CLFV processes in the muon sector will be a clear hint of New Physics. In case of no signal event observation, Mu2e will set a 90% upper limit on the ratio between the conversion and the capture rates $R_{\mu e} < 8 \times 10^{-17}$, improving the current best limit [3] by four orders of magnitude. The experimental signature searched in Mu2e is a single electron with energy slightly below the muon rest mass, that is $E_e = 104.97$ MeV.

As shown in Fig. 1 the Mu2e experiment is based on a system of three superconducting solenoids to enhance the number of negative muons arriving at the Stopping Target. An 8-GeV pulsed proton beam hitting the tungsten target inside the production solenoid (PS) produces mostly low-momentum pions. Thanks to the graded magnetic field, particles produced forward are reflected back toward the S-shaped transport solenoid (TS). This region allows having a very intense ($\sim 10^{10}$ μ/s) pure low-momentum negative muon beam at the entrance of the detector solenoids (DS) thanks to a middle collimator to select the particle charge. The DS houses the stopping target (made of 37 aluminum annular 105 μm

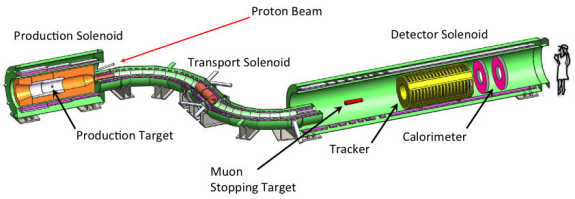

Fig. 1. Layout of the Mu2e experiment: PS, TS, and DS are indicated in the picture. The CRV, surrounding the DS and part of the TS, is not shown.

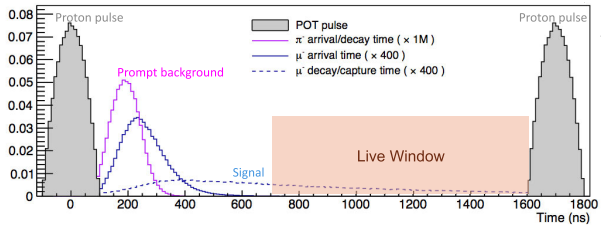

Fig. 2. Timing structure of the Mu2e beam.

thick foils, spaced 2.2 cm apart) and the detectors—a very precise ($\sigma_p = 200$ keV at E_e) straw tubes tracker [4] and an electromagnetic calorimeter [5]. The tracker is composed of ∼20 000 low mass, very thin, straw drift tubes and will measure the charged particle momenta reconstructing their trajectories in the B-field with the detected hits.

Within its lifetime the experiment plans to collect 6×10^{17} muon stops, necessary to reach its sensitivity goal. To reduce Cosmic Ray contribution, the external area of the DS, and part of the TS, are covered by a Cosmic Ray Veto (CRV) [6] system. Once muons are stopped in the Al target, they create muonic atoms and then cascade to the 1S ground state, with 39% decaying in orbit (DIO) and 61% captured by the nucleus. In the last case, due to the occurring nuclear processes, low-energy protons, neutrons, and photons are emitted, originating a large neutron flux as well as a large ionizing dose in the detectors.

To improve the current best limit by four orders of magnitude, Mu2e differs from earlier muon-to-electron conversion experiments in three major ways:

1) the muon beam intensity is 10 000 times greater than those of the previous experiments;
2) the presence of the TS, besides providing muon sign-selection, suppresses the neutral particles contribution at the entrance of the DS, allowing an efficient muon transport to the stopping target;
3) the pulsed structures of the beam and a delayed acquisition window: in order to suppress the prompt background, the muons hitting the stopping target are intended to be distributed in a narrow time burst (<200 ns) as shown in Fig. 2, with a bunch separation of ∼1.7 μs (i.e., larger than 826 ns, the muonic aluminum lifetime). Their decay products are observed only 700 ns after the proton arrival to make the prompt background negligible. These choices were guided by the observation that the result of the SINDRUM II experiment was ultimately limited by the need of suppressing the prompts.

The data-taking plan has been organized into two periods (Run I and RUN II), well separated by a two-year-long shutdown for the installation of PIP-II, the linac for the DUNE experiment. In Run I only 10% of the total number of protons on target (POT) will be produced. 75% of these POTs will be delivered with a low-intensity proton beam with a mean intensity of 1.6×10^7 protons/pulse, while the remaining 25% will be delivered in the high-intensity mode (3.9×10^7 protons/pulse).

II. Mu2e Electromagnetic Calorimeter

To validate the charged particle reconstructed by the tracker, the Mu2e calorimeter [7] provides information about its energy, timing, and position, adding particle ID capabilities to reject muons and antiprotons interactions mimicking the signal. In addition, the calorimeter is required to be also fast enough to provide a tracker-independent software trigger and help the tracks seeding [8].

To accomplish these requirements the calorimeter has to maximize the acceptance for ∼105 MeV/c conversion electron (CE) tracks, operate in a vacuum, survive in the "harsh" radiation environment and satisfy the experimental requirements discussed below.

A. Experimental Requirements

To fulfill the previously stated tasks, simulation guided us in defining the reconstruction requirements for 105 MeV electrons, which are summarized by this short list:

1) an energy resolution better than $\sigma_E/E = \mathcal{O}(10\%)$, to reach a rejection factor at the level of 200 between CE and the ∼40 MeV energy deposit from 105 MeV/c cosmic ray muons mimicking the signal [9];
2) a timing resolution better than ∼0.5 ns, to ensure that the energy depositions in the calorimeter are in time with the CEs reconstructed by the tracker and also improve the PID;
3) a position resolution $\sigma_{r,z} < 1$ cm, to match the position of the energy deposit with the extrapolated trajectory of a reconstructed track;
4) ability to survive the high radiation environment, maintaining its functionality for radiation exposures up to ∼15 krad/year in the hottest regions and for a neutron flux equivalent to 10^{12} $n_{1\,MeV}/cm^2$/year, inside an evacuated region (10^{-4} Torr) of the DS that provides 1 T axial magnetic field;
5) a fast enough response in order to handle the experimental high rate ($\tau < 40$ ns);
6) a temperature and gain stability within ±0.5%, not to deteriorate the energy resolution;
7) reliability and redundancy to operate in a vacuum for one year without any interruptions.

B. Technical Choice

In 2015, after a long Research and Development phase [10], [11] carried out to better define the detector, the final design of the Mu2e calorimeter was decided: a high-quality undoped CsI crystal calorimeter with silicon photomultipliers (SiPMs) readout and with a geometry organized in two annular disks.

Indeed, undoped CsI represents the best compromise between cost, reliability, performance, and radiation hardness, providing a fast emission time ($\tau = 30$ ns) and a sufficiently

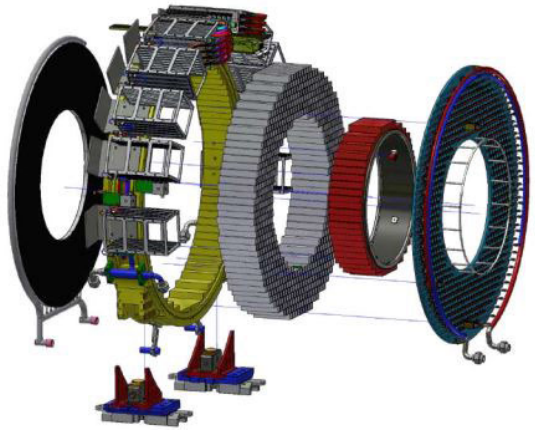

Fig. 3. Breakout of calorimeter mechanical components.

high Light Yield (∼2000 γ/MeV). To well match the scintillation emission of 310 nm to the SiPM photon detection efficiency (PDE), UV-extended Hamamatsu SiPMs with a front window made of silicon resin were selected. To operate in a vacuum and minimize outgassing contributions, the crystal-SiPM coupling was done without any optical grease.

In Fig. 3, the design of the calorimeter is shown: two annular disks with an inner (outer) radius of 35 cm (66 cm) and a relative distance of 70 cm, corresponding to the half pitch of the helical CE trajectory. Each disk is composed of 674-square-based scintillating crystals of 3.4 × 3.4 × 20 cm^3. Even if the crystal length is only 10 X_0, it is sufficient to contain the 105 MeV electron showers since the CEs impinge on the calorimeter surface with a ∼50 ° angle. To improve reliability, light collection, and resolution, each crystal is readout by two custom designed SiPMs array. Each one is a parallel configuration of two series of three 6 × 6 mm^2 monolithic sensors. The array dimension where selected to maximize the light collection, obtaining an active area of 1.8 × 1.2 cm^2 and keeping a small total capacitance—thanks to the parallel configuration—to achieve a signal width smaller than 200 ns.

Each crystal is wrapped with a 150 μm thick foil of Tyvek[1]. The front-end electronics (FEE) are mounted on the rear side of each disk on the SiPMS pins, while voltage distribution, slow control, and digitizer electronics are housed behind each disk in custom crates. Each FEE/SiPMs/Crystal system has its own independent powering and readout channel.

C. Mechanics

The calorimeter mechanical structure was designed to support the layout of the crystals by piling them up in a self-standing array organized in consecutive staggered rows. Each crystal array is supported by two coaxial cylinders. The inner cylinder must be as thin and light as possible in order to minimize the passive material in the region where spiraling background electrons are concentrated. The outer cylinder is as robust as required to support the load of the crystals (700 kg). Each disk has two cover plates. The plate facing the beam is made of carbon fiber to minimize the degradation of the

[1]Registered trademark.

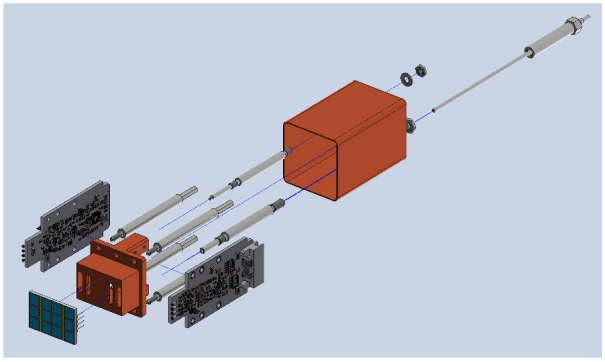

Fig. 4. Exploded view of the ROU components.

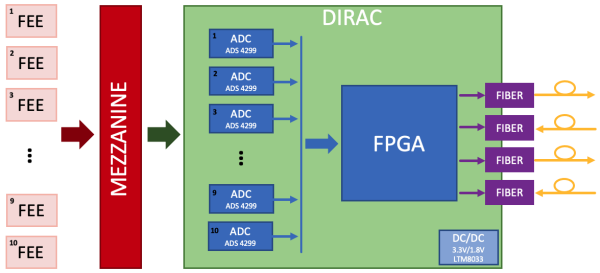

Fig. 5. Block diagram for the calorimeter waveform digitizer board, including also the MZB and the Amp-HV chips. The main components used are shown.

electron energy, while the back plate should also be robust to support the SiPMs, the FEE, and the SiPM cooling lines and it is therefore made of Polyether ether ketone (PEEK). The crystal arrangement is self-supporting, with the load carried primarily by the outer ring.

The heat generated by SiPMs, FEE, and readout electronics must be removed within temperature values acceptable for the correct operation of each device. Furthermore, the difficult access to components requires a cooling system free of faults and maintenance needs for at least 1 year. The cooling system has to maintain SiPM temperature at ∼−10 °C to minimize the dark current: this is obtained by choosing 3M NOVEC 123 HFE 1700) as refrigerating fluid, circulating at ∼−15 °C.

D. Electronics

The electronics is based on analog FEE cards directly connected to the SiPM pins and by a digital readout part distributed on crates surrounding the disk. As shown in Fig. 4, the FEEs are mounted on a copper support where the SiPMs are glued. In the following, the ensemble of these components will be called readout units (ROU).

FEEs provide amplification and shaping of the signals, and a local high voltage (HV) regulation for independent control of the bias voltages (through high-voltage ADCs and DACs). Readout of current and temperature sensors are also provided.

Data Acquisition and digitization are handled by a Mezzanine Board—controlling the HV and monitoring the current and temperature of SiPMs and a readout- and a digitizer readout controller (DIRAC) board—to perform the zero-suppression and sample the signals with 5 ns binning. Each digital board handles 20 channels. A schematic view of the FEE-MZB-DIRAC chain is shown in Fig. 5.

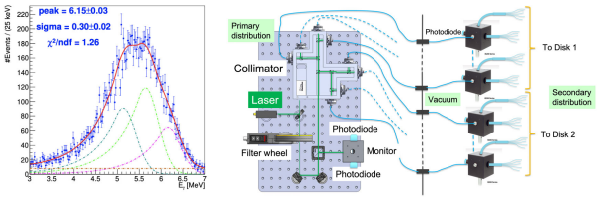

Fig. 6. Energy spectrum for a crystal irradiated with 6.13 MeV photons from the ^{16}O (left). Primary and secondary distribution laser system (right).

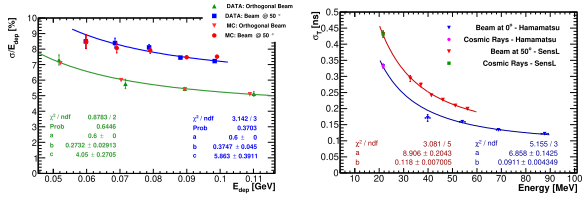

Fig. 7. Energy (left) and time (right) resolution obtained with the electron beam test performed at BTF.

E. Calibration and Performance Monitoring

The high sensitivity required by the Mu2e experiment implies special care in detector calibration to avoid any related systematic effects. A liquid radioactive [Fig. 6 (left)] source will provide an absolute energy scale and a fast response equalization between crystals. This system is similar to the one developed for the BaBar calorimeter [12]: a 6.13 MeV photon line is obtained from a short-lived ^{16}O transition. The decay chain comes from a Fluorinert[2] coolant liquid (FC-770) that is activated by fast neutrons produced by a DT generator. Continuous monitoring of gains and time offset for each channel is instead provided by a laser monitoring system [Fig. 6 (right)]: the laser light is distributed to each channel via a primary and a secondary distribution system, through an optical fiber whose final support is inserted inside the ROU structure as shown in Fig. 4.

III. Calorimeter Performance

To verify the selected design before starting the massive production of the whole calorimeter components, a large-size prototype was built and exposed to an electron beam at the Beam Test Facility of the National Laboratories of Frascati. Module-0 is composed of 52 undoped CsI crystals read out by 102 SiPM connected to FEE boards. Its mechanics was designed to resemble as much as possible that of the final calorimeter, allowing the test assembly procedures and cooling. A detailed description of the setup and the main results (reported in Fig. 7) obtained during the beam test can be found in [13]. For what concerns energy resolution, the function used to fit the data is

$$\frac{\sigma_E}{E} = \frac{a}{\sqrt{E[\text{GeV}]}} \oplus \frac{b}{E[\text{GeV}]} \oplus c \tag{1}$$

the dominant term was the constant term c due to leakage, the stochastic term a was consistent with a light yield of $\mathcal{O}(20$ pe/MeV/SiPM), the noise term b was dominated by an electronic noise of $\mathcal{O}(400)$ keV/channel and a coherent noise related to the used digitizers. Runs at an angle were also performed to study the performance expected with CE; due to longer clusters and higher transversal leakage the linear and constant term increased. An energy resolution better than 5 (7.5)% was achieved at 100 MeV for runs at normal (at 50 °) incidence.

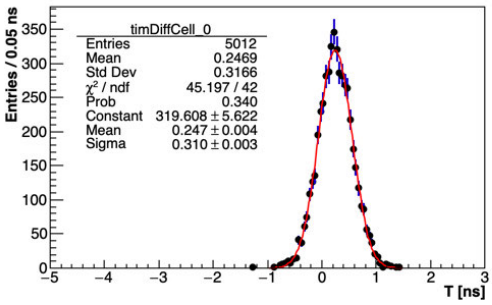

Fig. 8. Timing resolution of a single crystal of the large area prototype.

The time resolution was evaluated as the difference between the time of the two SiPM coupled to the same crystal, obtaining a timing resolution better than 200 ps at 100 MeV. The fit function used for the time resolution is

$$\sigma_T = \frac{a}{E[\text{GeV}]} \oplus b \tag{2}$$

where a is proportional to the emission time constant of the undoped CsI and b represents the additional contribution due to the readout electronics. In the years following the test beam, Module-0 has continuously operated to study the behavior in a vacuum, at low temperatures as well as for carrying out vertical slice tests of increasing complexity, at a Cosmic Ray test stand where the timing calibration algorithms were improved. The timing resolution obtained subtracting time of two SiPMs reading the same crystal is reported in Fig. 8.

IV. Calorimeter Production Status

A. Crystal and SiPMs Characterization

The physics requirements previously discussed were used to define a set of technical specifications for the undoped CsI crystals and SiPMs. The selection criteria to accept crystals were: 1) a Light Yield LY $>$ 100 p.e./MeV; 2) an energy resolution better than 20% at 511 keV; 3) a longitudinal response uniformity (LRU), defined as the rms of the LY measured in eight or more points along the longitudinal axis, below 5%; and 4) a ratio between fast and total light yield components (F/T) above 75%. 1450 Undoped CsI crystals were produced by Siccas [14] and Saint Gobain [15]. Results of the optical properties measurements are reported in Fig. 9. As shown in Fig. 10 top, the results from the optical measurements were well in agreement with the specification for both vendors but Sain Gobain evidenced some difficulties in matching the 100 μm precision on the dimensions. A few, randomly selected, crystals were exposed to neutron and photon flux, and the Light Yield degradation observed remained between the limit set by the required specifications.

The specification for the Mu2e photosensors were: 1) a PDE larger than 20% at 315 nm; 2) a gain larger than 10^6 at the operational voltage $V_{\text{op}} = V_{\text{br}} + 3$ V; 3) a recovery time (τ) smaller than 100 ns for each of the 6 $\times$ 6 mm^2 cell, when measured on a load larger than 15 Ω; 4) a maximum acceptable operation voltage spread among the six SiPMs cells of ±0.5%;

[2]Trademarked.

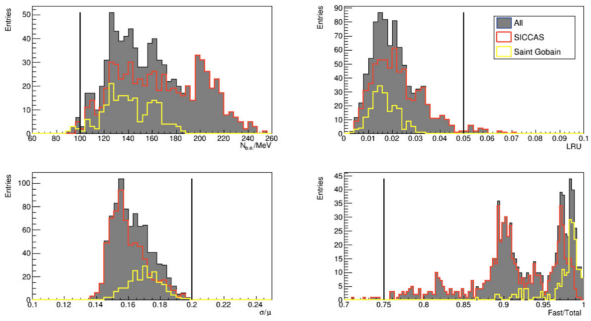

Fig. 9. Number of photoelectrons (top left), LRU (top right), energy resolution (bottom left), and fast over total ration (bottom left) distributions for Saint Gobain (yellow) and Siccas (red). The cumulative distributions are reported in gray. The black lines represent the experiment requirements.

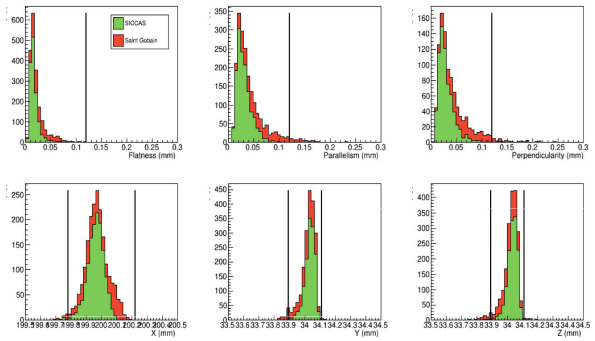

Fig. 10. Results of the CMM measurements on the production crystals. Flatness (top left), parallelism (top center), and perpendicularity (top right) and the X (bottom left), Y (bottom center), and Z (bottom right) dimensions. The black lines represent the requirements.

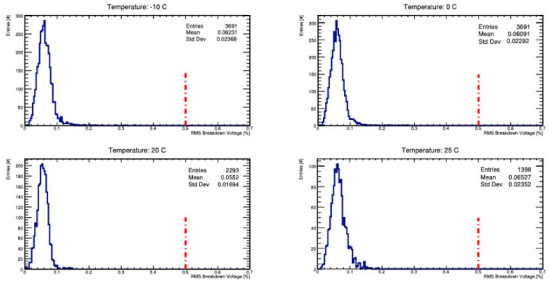

Fig. 11. RMS of the breakdown voltage test of each cell of the SiPMs. The results are reported for the three different temperatures tested. The red lines represent the limits on acceptable values.

and 5) a maximum acceptable dark current (I_{dark}) spread at V_{op} among the six SiPMs cells of ± 15 %; 6) I_{dark} smaller than 10 mA at operation voltage and a gain reduction smaller than a factor of 4 while irradiating SiPMs up to 3×10^{12} $n_{1\,\text{MeV}}/\text{cm}^2$ at 20 °C; 7) a Mean Time To Failure (MTTF) better than a million hours while operating at 0 °C.

As already stated 4000 Mu2e SiPMs (considering also spares) were produced by Hamamatsu [16]. Each monolithic cell of the SiPMs was tested to measure the operational voltages (V_{op}), the dark current at V_{op} and the product of Gain × PDE in a custom test stand. Some of the results obtained can be seen in Fig. 11.

A random sample of SiPMs was selected to be irradiated with neutron fluence up to $\sim 10^{12}$ $n_{1\,\text{MeV}}/\text{cm}^2$ while other SiPMs were selected to evaluate their Mean Time To Failure. To test an MTTF at the level of 10^6 h, the SiPMs under test

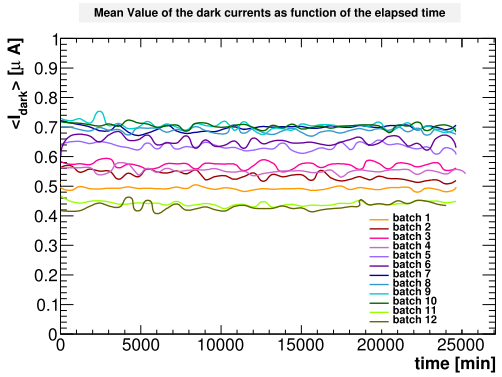

Fig. 12. Mean value of the currents of 15 SiPMs as a function of the elapsed time during the MTTF test. The different line colors refer to different batches tested.

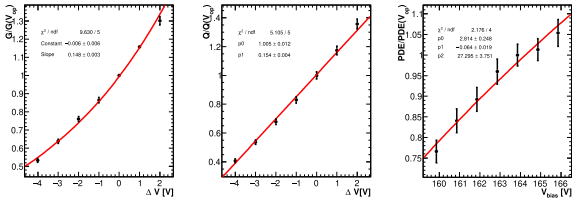

Fig. 13. Example of the results of a seven points scan for gain, collected charge, and PDE. All values are normalized to the results at Vop. G and Q are shown as a function of the overvoltage, while the PDE versus V_{bias}.

were kept in operation in a dedicated box at 65 °C for 342 h. At the end of the test, no failures were observed thus allowing us to estimate a MTTF $> 10^7$. Results of the test are reported in Fig. 12.

B. Front-End Electronics

The FEE boards have to provide: 1) a signal rise time of ∼25 ns to allow an appropriate time reconstruction; 2) a rate capability up to 1 MHz and a short fall time; 3) a radiation-hardness for up to 100 krad and 10^{12} $n_{1\,\text{MeV}_{\text{eq}}}/\text{cm}^2$); 4) a programmable bias voltage up to 200 V via a 12-bit DAC; and 5) the possibility to set SiPM bias and to monitor current and temperature via a 12-bit ADC.

The FEE boards were produced by ARTEL [17] with a negligible rejection factor albeit all 2500 boards underwent a burn-in test at 65 °C in a climatic chamber in JINR (Dubna, Ru), followed by a calibration phase for both HV, gain and differential linearity parameters. After assembling the FEE on the copper support for the Mu2e SiPMs, a characterization of the entire ROU is performed to evaluate the gain, charge, and PDE dependence on the bias voltage (Fig. 13) in a region around $(-4 \div +2$ V) the operational voltage.

At the moment of writing 1150 out of 1500 ROUs (1348 for the disks, plus spares) have been already assembled and more than 1000 fully characterized. In Fig. 14 the gain at the operational voltage for all the tested ROUs is reported.

C. Dark Current Control at the End of Data Taking

A small sample of 50 SiPMs—randomly selected during the production—were exposed unbiased to a neutron fluence of $\sim 10^{12}$ $n_{1\,\text{MeV}}/\text{cm}^2$ at the EPOS [18] facility of Helmholtz-Zentrum Dresden-Rossendorf (HZDR). The I_{dark} increase was measured once the SiPMs were brought back to Fermilab.

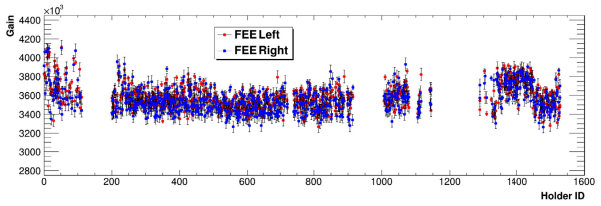

Fig. 14. Gain distribution with respect to the Holder ID. The gain for the left and right SiPM-FEE couples is plotted separately for each holder.

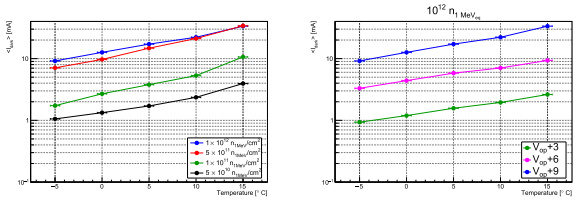

Fig. 15. Mean value of the leakage current as a function of the SiPMs temperature for SiPM irradiated at different neutron fluences (red curve: 10^{12} $n_{1\,MeV_{eq}}$, blue curve: 5×10^{11} $n_{1\,MeV_{eq}}$, green curve: 10^{11} $n_{1\,MeV_{eq}}$, black curve: 5×10^{11} $n_{1\,MeV_{eq}}$) (left). I_{dark} dependence on SiPM temperature for different overvoltages (right).

To better characterize the response of irradiated SiPMs, and further verify the final calorimeter operational temperature, a total of 35 SiPMs were irradiated at the ENEA Frascati Neutron Generator (FNG) [19], using a 14 MeV neutron gun based on T(d,n)α fusion with neutron fluences ranging from 5×10^{10} up to 1×10^{12}.

After the irradiation, the measurement of I–V curves was performed at different temperatures (+15 °C, +10 °C, +5 °C, 0 °C, and −5 °C) to evaluate the SiPM operational voltage and the dark current at V_{op}. In Fig. 15, some of the results obtained with the SiPMs irradiated at FNG are reported. Among all the samples, we conservatively selected only samples with higher leakage current. In Fig. 15 (left) the leakage currents measured at V_{op} at different temperatures and fluences are reported: the dependence of I_{dark} to the sensor temperature appears to be linear and a factor of ∼2 decrease in leakage current is observed when reducing the temperature by +10 °C. Looking at Fig. 15 (right), that represents the leakage current dependence on the temperature at fluence compatible to the lifetime of the experiment, for different bias voltages (V_{br} + 3, V_{br} + 6, V_{br} + 9), it is clear that the calorimeter will need to operate the SiPMs down to −10 °C, in order to meet the 2 mA limit on each channel, assuming only a small decrease in V_{bias}.

D. Calorimeter Assembly at Fermilab

According to the current schedule, it is planned that the calorimeter will be installed in the experimental hall by summer 2024 and all the service lines will be completed by the autumn of that same year. Soon after, a commissioning data-taking with cosmic rays will start, while waiting for the tracker to be installed. To respect this schedule, the disks have to be assembled by the spring of 2023.

Within the last two years, all large mechanical parts (see Fig. 16) have been produced. Before shipping them to Fermilab, a dry-fit was carried out in a clean room at Laboratori Nazionali di Frascati (LNF) to check that all pieces were well fitting as shown in Fig. 16. A careful vacuum leak test was performed both on the crate manifolds and on the elbow joints between crates and manifolds: a maximum leak rate of 10^{-10} atm × cc/s was achieved, satisfying the experiment requirements.

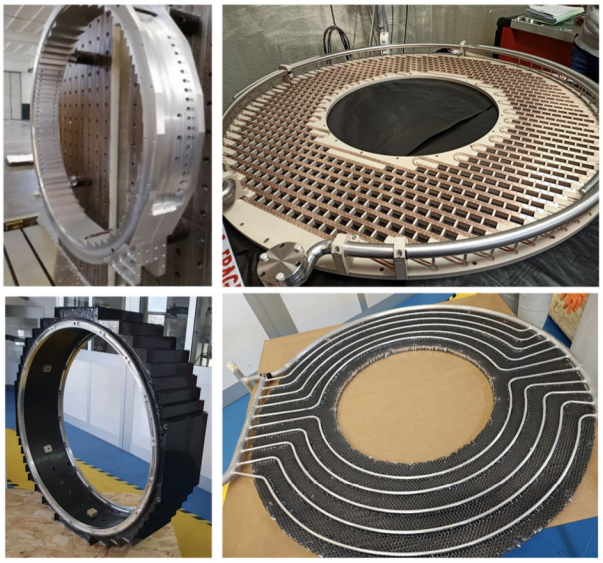

Fig. 16. Calorimeter mechanical parts: outer ring (top-left); FEE plate (top-right); inner ring (bottom-left); and front plate with source tubing embedded in the aluminum honeycomb (bottom-right).

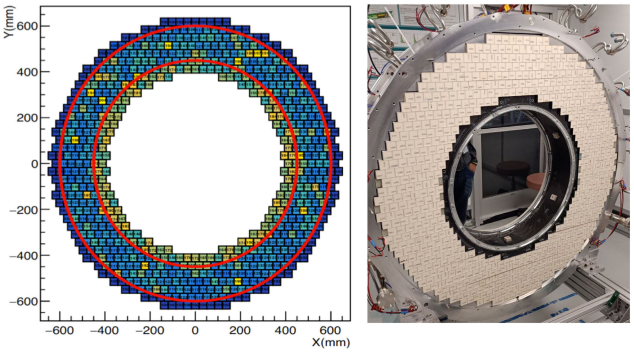

Fig. 17. Distribution of the LY in photoelectrons/MeV (left) and down-stream disk filled with 674 crystals (right).

At the moment, the down-stream disk (Disk1) is under assembly at the Silicon Detector facility (SiDet) at Fermilab in a clean room (ISO 7), while the up-stream disk (Disk0) has all the mechanical parts assembled at LNF and is still waiting to be shipped to Fermilab. The Disk1 assembly at SiDet started in June 2022 with the installation and alignment of the Outer Ring over its stand and progressed with the Inner Ring alignment. 674 crystals, among the over 1450 wrapped in Tyvek[1] and fully characterized with a source, were selected to be stacked in the downstream disk. Before stacking, a set of two day long outgassing runs was performed in a dedicated vacuum vessel to reduce the residual single crystal outgassing level below 10^{-4} Torr l/s. The positioning of the crystals in the disk was carefully optimized, taking into account optical, mechanical, and radiation hardness properties. Three areas have been identified as a function of the expected level of total ionizing dose (TID), occupancy, and resolution, considering that TID and occupancy decrease radially moving toward the outermost part of the disk. The chosen crystal distribution is shown in Fig. 17.

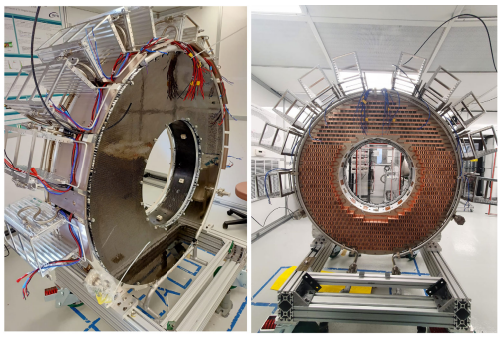

Fig. 18. Front and rear face of the down stream disk of the Mu2e calorimeter.

A 50 μm thick Tedlar[1] layer was placed between each stacked row; to keep the crystal matrix solidly connected, each row was then compressed using screws pushing on plastic shims at both row ends. A high precision bubble level allowed to check the accuracy of stacking procedure, which was later reconstructed offline after an overall survey with a laser tracker.

Starting in fall 2022, the front panel with an embedded source was installed and coupled to the Carbon Fiber Inner Ring and the outer Al disk. Subsequently, the ten crates supporting the mezzanine and DIRAC board, as well as the connection to the cooling circuits, were installed and the possible losses were carefully tested with a Helium sniffer, proven to be lower than 10^{-11} Torr $\times$ l/s.

The first 500 ROUs were received at Fermilab in September 2022. An outgassing campaign of these ROUs started in October 2022 to reduce their outgassing level below 10^{-4} Torr l/s before inserting them in the FEE disk. In Fig. 18 the current status of the assembly is shown.

V. Conclusion

In this article, the construction status of the Mu2e electromagnetic calorimeter is summarized. The detector is composed of two annular disks, each filled with 674 pure CsI crystals. Each crystal is coupled to two custom UV-extended SiPMs, to provide redundancy.

While the production of crystals, SiPMs, and FEE boards has been completed, digital electronics production is still underway. The assembly of the ROU, each one composed of two SiPMs and two FEE units, is more than 70% complete and a full characterization of the gain, and of the gain dependence on bias voltage, is being successfully carried out. This calibration will allow to adjust the calorimeter response once in operation and after the detector will be exposed to a large neutron fluence. Knowing this behavior "apriori" will be pivotal when the neutron fluence will cause an increase of the SiPMs dark current. To keep the leakage current of each channel under the 2 mA limit set by the read-out board, it will be possible either to decrease the operating temperature of the SiPMs or reduce the bias voltage.

At the moment of writing all mechanical parts of the calorimeter have been delivered and the downstream disk is under assembly at Fermilab. The calorimeter support structure has been completed and all crystals are stacked. The mounting of the ROU is started with more than 2/3 being inserted in their own position in the readout plate. It is expected to conclude this part of the assembly by the end of 2022 and then repeat the same steps for the other disk.

Finally, as soon as the digital electronics will be delivered, we plan to complete an integrated test of the calorimeter readout starting in summer 2023 before getting ready to move the calorimeters into the experimental hall.

Acknowledgment

The authors are grateful for the vital contributions of the Fermilab staff and the technical staff of the participating institutions. This document was prepared by members of the Mu2e Collaboration using the resources of the Fermi National Accelerator Laboratory (Fermilab), a US Department of Energy, Office of Science, HEP User Facility.

References

[1] L. Bartoszek et al., "Mu2e technical design report," 2015, *arXiv:1501.05241*.
[2] S. M. Bilenky, S. T. Petcov, and B. Pontecorvo, "Lepton mixing, $\mu \rightarrow e + \lambda$ decay and neutrino oscillations," *Phys. Lett. B*, vol. 67, no. 3, pp. 309–312, 1977.
[3] W. Bertl et al., "A search for μ-e conversion in muonic gold," *Eur. Phys. J. C*, vol. 47, no. 2, pp. 337–346, Aug. 2006.
[4] M. J. Lee, "The straw tube tracker for the Mu2e experiment," *Nucl. Part. Phys. Proc.*, vols. 273–275, pp. 2530–2532, Apr. 2016.
[5] N. Atanov et al., "Design and status of the Mu2e calorimeter," *IEEE Trans. Nucl. Sci.*, vol. 65, no. 8, pp. 2073–2080, Aug. 2018.
[6] A. Artikov, "Performance of scintillator counters with silicon photomultiplier readout," 2015, *arXiv:1511.00374*.
[7] N. Atanov et al., "The Mu2e calorimeter final technical design report," 2018, *arXiv:1802.06341*.
[8] G. Pezzullo and P. Murat, "The calorimeter-seeded track reconstruction for the Mu2e experiment at fermilab," in *Proc. IEEE Nucl. Sci. Symp. Med. Imag. Conf. (NSS/MIC)*, Oct. 2015, pp. 1–3.
[9] M. Collaboration, "Mu2e run I sensitivity projections for the neutrinoless $\mu^- \longrightarrow e^-$ conversion search in aluminum," *Universe*, vol. 9, no. 1, p. 54, Jan. 2023.
[10] N. Atanov et al., "Measurement of time resolution of the Mu2e LYSO calorimeter prototype," *Nucl. Instrum. Methods Phys. Res. A, Accel. Spectrom. Detect. Assoc. Equip.*, vol. 812, pp. 104–111, Mar. 2016.
[11] N. Atanov et al., "Energy and time resolution of a LYSO matrix prototype for the Mu2e experiment," *Nucl. Instrum. Methods Phys. Res. A, Accel. Spectrom. Detect. Assoc. Equip.*, vol. 824, pp. 684–685, Jul. 2016.
[12] B. Aubert et al., "The BABAR detector," *Nucl. Instrum. Methods Phys. Res. A, Accel. Spectrom. Detect. Assoc. Equip.*, vol. 479, pp. 1–116, Feb. 2002.
[13] N. Atanov et al., "Electron beam test of the large area Mu2e calorimeter prototype," *J. Phys. Conf. Ser.*, vol. 1162, no. 1, 2019, Art. no. 012027.
[14] *Siccas Website*. Accessed: Mar. 7, 2023. [Online]. Available: http://www.siccas.com
[15] *Saint Gobain Website*. Accessed: Mar. 7, 2023. [Online]. Available: https://www.crystals.saint-gobain.com
[16] *Hamamatsu Website*. Accessed: Mar. 7, 2023. [Online]. Available: https://www.hamamatsu.com
[17] *ARTEL Website*. Accessed: Mar. 7, 2023. [Online]. Available: www.artel-srl.com
[18] R. Krause-Rehberg, *The EPOS System at the Radiation Source ELBE at Forschungszentrum Dresden-Rossendorf*. (Physics With Many Positrons). Amsterdam, The Netherlands: IOS Press, 2010, pp. 463–479.
[19] *FNG Website*. Accessed: May 20, 2023. [Online]. Available: https://www.enea.it/it/ateco/schede/impianto-generatore-di-neutroni-fng